Intelligent Control and System Engineering 2023; 1(1): 315.
Original Research Article

Full vector intelligent detection of cigarette appearance based on machine vision

Shifei Jiang[1,2], Zhaoguo Zhang[1], Faan Wang[1,*], Zhi Li[2], Kaiting Xie[1], Chenglin Wang[1], Jinhao Liang[3]

[1] *Faculty of Mechanical and Electrical Engineering, Kunming University of Science and Technology, Kunming 650500, Yunnan Province, China*

[2] *Yunnan Tobacco Machinery Co., Ltd., Kunming 650100, Yunnan Province, China*

[3] *Department of Civil and Environmental Engineering, National University of Singapore, Singapore 119077, Singapore*

*** Corresponding author:** Faan Wang, wfa@kust.edu.cn

ARTICLE INFO

Received: 10 December 2023
Accepted: 26 December 2023
Available online: 6 February 2024

doi: 10.59400/icse.v1i1.315

ABSTRACT: As the final output product of tobacco agriculture, the appearance quality of cigarettes is the key link to control. However, there is no special detection equipment for the whole appearance defect detection of tobacco, while it mainly depends on manual detection, leading to the test standard is not unique and the test data cannot be stored effectively. In this research, the shape characteristics and appearance inspection requirements of cigarettes were analyzed with the black-box method. Then, a kind of cigarette appearance quality inspection equipment was designed, and the experimental data of the equipment was analyzed with Design-Expert11. The results show that the device can image the appearance of a cigarette completely. The optimum parameters of the equipment are: the lifting speed of slide plate is 0.3 m/s, the angle of transition plate is 40°, the displacement speed of roller is 0.045 m/s, the movement speed of the slide plate is 0.4 m/s, the expansion speed of the cylinder is 20 mm/s, the spring coefficient is 3 n/s, the angle of the light source is 10°, and the height difference between the light source and the cigarette is 30 mm. The equipment can meet the needs of cigarette appearance detection and provide a reference for cylindrical object appearance detection.

KEYWORDS: visual detection; cigarette appearance; full vector detection; convolutional neural network; cylindrical object detection

1. Introduction

Tobacco is one of the most important special agricultural crops, and the tobacco economy is related to the national people's livelihood[1]. As the final tobacco product, it is equally important that their appearance quality gives people a visual experience while cigarettes have high-quality internal qualities. At present, the detection of cigarettes mainly relies on manual work, resulting in problems such as inconsistent detection standards and the inability to store detection data electronically in real-time. Combined with the actual needs of industrial production and the theoretical basis of visual technology, non-manual detection technology has been researched a lot by many relevant scholars. For example, the model for improving detection accuracy is continuously upgraded[2]. The convolutional layer, pooling layer, and activation function of the convolutional neural network (CNN) are improved to improve the ability of object detection[3,4]. Through the broadening technique of sample data, the overfitting caused by insufficient training label data is alleviated[5]. The improvement of optical illumination technology, image

acquisition, image processing, and image analysis technology provides basic data conditions for machine vision inspection[6]. Lightweight inspection models are being researched to make inspections faster[7], Convolutional neural networks are used to detect and track moving objects[8,9]. The research on the integration of vision technology and deep learning algorithms has made object detection technology fruitful and technologically advanced. For example, the combination of structured light imaging and visual recognition models is utilized for weld seam surface quality inspection[10]. Tian et al.[11] proposed a distance field model with semantic segmentation for automatic recognition of food labels, which effectively improves the accuracy of food label detection. Zhao[12] proposed an image region extraction algorithm to achieve efficient detection of defects such as missing, damaged, cracked, and faded sugar coating of Chinese medicine grains in pharmaceutical packaging. Xiao and Qiu[13] proposed a combination of local histogram equalization and linear enhancement based on double Gaussian second-order derivation, which achieved high accuracy and solved the problem that thin sheets are difficult to count. Madessa et al.[14] proposed an instance segmentation method based on deep learning features, which improved the detection ability of transparent materials. Liu et al.[15] designed a visual detection method for foreign bodies at the groove of zirconium tubes based on the average template method, which can effectively and accurately detect small-sized foreign bodies at the grooves of zirconium tubes. Deng and Pu[16] extracted lane feature points by fusing edge detection and multi-color space threshold segmentation results, which achieved high accuracy of lane line detection under complex working conditions. Chen et al.[17] proposed a migration learning-based improved mobilenetV2 lightweight network for packaging defect detection, which achieves fast and high-precision detection[17], rapid non-destructive determination of physicochemical values based on Vis/NIR spectroscopy for potato late blight detection is implemented by combining visible/near-infrared (Vis/NIR) spectroscopy with machine learning (ML)[18], which solved the problem of low accuracy of detecting internal and external defects in potatoes. Zhang et al.[19] improved the YOLOV4 model to achieve efficient detection of potato mechanical damage in complex environments.

Cigarettes have the shape characteristics of a cylinder, so the acquisition and detection of their appearance images are different from that of flat images. Object detection with cylindrical features is a fundamental issue. Jiang et al.[20] proposed an image acquisition method for the cylinder block indicating the cross-hole, and utilized the machine vision method for its defect detection, resulting in high detection accuracy. Xu[21] conducted research on the defect visual detection algorithm for cylindrical product labels. Liu[22] conducted design and experimental research on the full-appearance visual inspection system of rotary body parts. At present, the research of deep learning algorithms is focused on object detection with cylindrical shape features, but the research results of image acquisition devices and defect detection equipment for cigarettes with cylindrical features have rarely been published.

In this paper, a machine with cigarette image acquisition and visual inspection is designed, and the key mechanisms are tested to obtain parameter combinations, which can enable smooth and lossless transmission of cigarettes and obtain high-quality images. The cigarette defect recognition ability and defect classification accuracy were verified, which provided the reference for the visual inspection of cylindrical objects.

2. Materials and methods

2.1. Material properties of cigarette

As an agricultural product, cigarette has the appearance characteristic of being cylindrical and physical properties such as low density and low hardness. The physical parameters of cigarettes are

shown in **Table 1**.

Table 1. Physical parameters of cigarette.

Physical item	Values
length/(mm)	84–120 (±0.5)
diameter/(mm)	5.4–7.8 (±0.1)
density of cigarette/(mg/cm³)	220–240 (±5)
weight/(mg)	600–900 (±21)
suction resistance/(Pa)	1100–1600 (±120)
hardness/(%)	60–70 (±8)
perimeter/(mm)	17–24.5 (±0.2)

2.2. Analysis of the technical system and structure of the whole machine

2.2.1. Analysis of technical system

The black box method[23] was used to analyze the cigarette detection technology system. The input of the material flow is cigarette sticks, and the output is cigarette sticks that have been photographed. The input of the energy flow is electrical energy, which is converted into mechanical energy to provide power for every mechanical action, The input of the signal flow is the acquisition signal and the output is the image. The associated input is mechanical vibration, and its corresponding output is noise. The system analysis is shown in **Figure 1**.

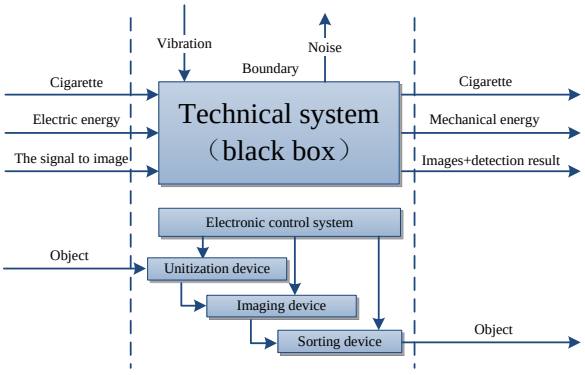

Figure1. Analysis diagram of the technical system.

The requirements for black boxes for technical systems are analyzed as follows. The process flow of the technical system should include the input of the object to be detected, machine vision inspection, and classification for input. The machine vision inspection part needs to meet the comprehensive inspection and non-destructive testing of the object at the same time. In terms of full-appearance inspection, the inspected object is required to be unitized first and then imaged on the full surface. During the photographing process, the outer surface of the detected object cannot be clamped and adsorbed, resulting in occlusion. The object needs to run smoothly during the conveying process and testing process to avoid secondary damage.

2.2.2. The structure and working principle of the whole machine

Cigarette appearance inspection equipment includes cigarette storage device, cigarette unitization device, cigarette full-appearance imaging device, sample sorting device and electronic control system. The working principle of the machine is as follows. Cigarettes are stored in batches in a cigarette

storage device, which is connected to the unitization device by a belt. The stacked cigarettes are discretized by the cigarette unitization device and outputted to the cigarette full-appearance imaging device. In the full-appearance imaging device of the cigarette stick, the cigarette stick is fully presented and imaged in an orderly and non-destructive manner. The sorting device is connected to the tail end of the full-appearance imaging device of the cigarette. After the cigarette photos are processed by the convolutional neural network model, the recognition signal is sent to the sorting device, which works to separate the defective cigarette from the normal cigarette. The electronic control system systematically controls the functions of each component and finally achieves the purpose of defect identification, defect classification, and sample sorting of cigarettes. The design of the whole device is shown in **Figure 2**.

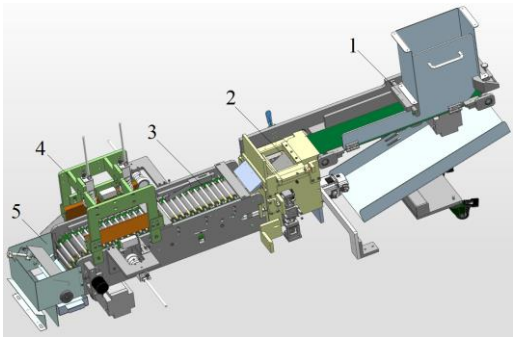

Figure 2. Schematic diagram of cigarette appearance detection equipment; 1: cigarette storage device; 2: cigarette unitization device; 3: full-appearance imaging device; 4: assembly of camera and light; 5: sorting device.

2.3. Structural design of the main institutions

2.3.1. Design of full-appearance imaging device

In this paper, rollers rotating in the same direction are designed, and cigarettes are placed between the rollers. Driven by the friction of the rotating roller group, the cigarette rotates, and its circumferential surface is fully presented, which avoids the problem of the surface being blocked under the conventional photographic method. Considering the efficiency of the inspection work, the roller needs to continue to walk when inspecting the cylindrical swivel body. While the roller rotates, it also needs to be displaced in the horizontal straight direction, forming an assembly line to work. Therefore, the two movements of roller rotation and horizontal linear motion need to be finished at the same time. The roller is innovatively designed as a structure in which the outer circumferential surface rotates relative to the central axis, and the central axis moves in a linear manner, to achieve the simultaneous conduct of linear movement and rotation of the roller. The roller design is shown in **Figure 3**.

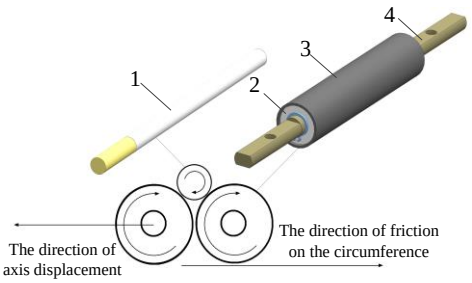

Figure 3. Schematic diagram of roller slewing mechanism; 1: cigarette; 2: bearing; 3: roller; 4: rotating shaft.

The roller movement can be reciprocating linear motion or cyclic circular motion. The compound

linear movement can be completed by the linear guide rail, and the transmission process has the characteristic of high precision and low noise. This method can reduce the influence of transmission on the image acquisition of the detected object, but it occupies a large space and takes a long time to reciprocate. The circular motion can be completed by a flexible belt, which has the advantage of fast cycle speed and high efficiency, and its disadvantage is that the belt transmission accuracy is low, which may affect the quality of imaging. Combining the advantages of the two methods, the cyclic circular motion is optimized to reduce the vibration of the imaging position. The mechanism principle is shown in **Figure 4**.

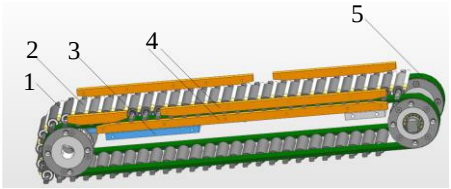

Figure 4. Design of motion model of Roller slewing mechanism; 1: cigarette; 2: roller; 3: friction plate; 4: guide bar for a limit; 5: circulating conveyor belt.

The quality of images is mainly affected by the relative position relationship between the light source and the object to be inspected. The parts to be inspected of the cigarette include the cylindrical arc surface and the two ends of the cylinder. The diffuse reflection effect caused by arc surface features and rough features helps improve imaging quality. Therefore, the requirements for the light source are to evenly light the surface of the arc to avoid bright spots or dark spots, which will affect the recognition of the image. The camera above the cigarette collects an image of the circumferential surface of the cigarette, cameras are set at both ends of the cigarette to acquire cross-sectional images of it. For the smooth circumferential surface of the cigarette, the direction of light source irradiation should be at a small angle to the horizontal plane, and the angle range is 0°–20°. The height difference between the light source and the cigarette can be adjusted. In this paper, 0°, 10°, 20°, and different heights were selected for combined comparison experiments. The structural relationship is shown in **Figure 5(a)**. The rough tobacco end face is easy to light and image, and the light source irradiation direction and end face are in the range of 0°–30°. The structural relationship is shown in **Figure 5(b)**.

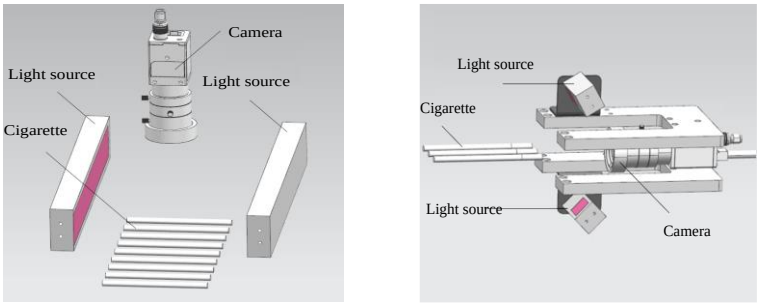

(a) **(b)**

Figure 5. The cooperation relationship between camera and light source; **(a)** circumferential form; **(b)** end form.

The cigarette stick is located between the rollers, and its gravity can be decomposed into radial pressure on the two rollers, forming friction between each other. The relationship between the roller and the cigarette is shown in **Figure 6**.

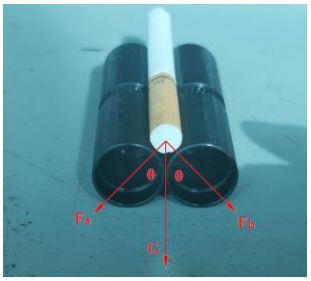

Figure 6. The relationship between roller and cigarette.

The relationship is established according to the mechanical analysis as follows:

$$F_a = F_b = G \times \cos\theta \tag{1}$$

The dynamic friction between the cigarette stick and the roller is expressed as:

$$F_{\mathrm{u}} = F_a \times \mathrm{u} + F_b \times \mathrm{u} \tag{2}$$

$$F_{\mathrm{u}} = G \times \cos\theta + G \times \cos\theta = 2G \times \cos\theta \tag{3}$$

where, F_a and F_b are the radial pressure of the cigarette on the two rollers respectively, N; G is the gravity of the cigarette, N; θ is the angle between the direction of gravity and of radial pressure, (°); F_{u} is the friction between the cigarette stick and the roller, N; u is the coefficient of friction between the cigarette stick and the roller.

The cigarette stick is driven by the rotation of the roller to move horizontally. The motion relation of roller slewing mechanism is shown in **Figure 7**. During the dynamic movement, the position relationship between the roller and the cigarette branch is as follows:

$$S_1 = S_2 = \pi \mathrm{D} \times n_1 = \pi \mathrm{d} \times n_2 \tag{4}$$

$$V_1 = V_2 = W_1 \times \pi \mathrm{D}/360 = W_2 \times \pi \mathrm{D}/360 \tag{5}$$

where, S_1 is the horizontal displacement of the roller, m; S_2 is the horizontal displacement of the cigarette, m; W_1 is the angular velocity of the roller, rad/s; W_2 is the angular velocity of the cigarette, rad/s; V_1 is the moving speed of the roller, m/s; V_2 is the moving speed of the cigarette, m/s; n_1 is the number of rotations of the roller; n_2 is the number of rotations of the cigarette.

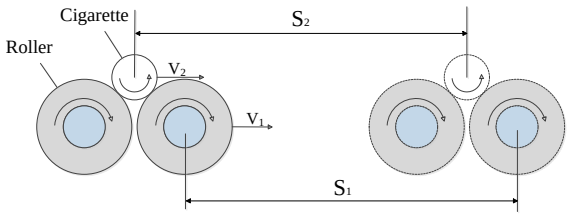

Figure 7. Motion parameter relation of Roller slewing mechanism.

During the image acquisition process, several image acquisitions are required to fully cover the circumferential surface of the cigarette. In this paper, cigarette image acquisition was completed through three images, each of which contained a circumferential surface larger than 120 degree. While the cigarette at first camera shooting position is recorded as the zero position, the cigarette position of the second imaging station is expressed as follows:

$$S' = n \times \pi \mathrm{d} + \pi \mathrm{d} \times 120/360 \tag{6}$$

When the cigarette at the third station is photographed, its location is as follows:

$$S'' = n \times \pi d + \pi d \times 240/360 \tag{7}$$

where, S' is the distance between zero point and the cigarette at the second imaging location, m; S'' is the distance between zero point and the cigarette at the third imaging location, m; d is the diameter of the cigarette, m; n is an integer.

During the mutual movement of the cigarette and the roller, the condition for the complete imaging of the surface of the cigarette stick is that the transmission between the roller and the cigarette stick is stable, and the cigarette cannot slip. The linear velocity of the roller surface is equal to that of the tobacco surface, there should be a relationship between the roller and the cigarette described in Equations (4) and (5), which means $V_1 = V_2$, $S_1 = S_2$.When the cigarette is at the zero position $V_1 = 0$, $W_1 = 0$. The position relation between the cigarette and the camera is shown in **Figure 8**. Under the action of friction, the speed of the cigarette branch is gradually synchronized with that of the roller, and during this movement, the frictional movement of the cigarette has the following relationship:

$$V_t = V_0 + at \tag{8}$$

$$a = F/m \tag{9}$$

$$F = m \times g \times u \tag{10}$$

The following formula can be deduced:

$$V_t = V_0 + g \times u \times t \tag{11}$$

When the cigarette is at the zero position,

$$V_0 = 0,\ V_t = g \times u \times t \tag{12}$$

where V_0 is initial speed of cigarette, m/s; V_t is the speed at t moment, m/s; a is acceleration, m/s^2; m is the quality of the cigarette, kg; g is the acceleration of gravity, m/s^2; u is the coefficient of friction.

Until the cigarette reaches the same linear velocity as the roller, there is slippage between the cigarette and the roller and no valid image can be acquired. Therefore, the following conditions should be met between the first imaging position and the initial position of cigarette:

$$S_0 > V_2 \times t \tag{13}$$

where S_0 is the distance between the first imaging position and the initial position of the cigarette, m; V_2 is the linear velocity of the roll surface, m/s; t is the time taken for cigarette to reach the same speed with rollers.

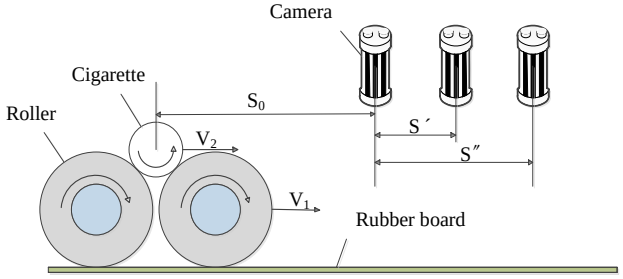

Figure 8. The position relation between the cigarette and the camera.

2.3.2. Design of cigarette unitization device

In order to achieve the full appearance inspection of the cigarette, the cigarette must be presented in the form of a unit. According to the cylindrical characteristics of cigarettes, a unitizing device with

universal applicability is designed. The cam mechanism is used to realize the unitization of cigarettes. The rotation of the wheel drives the eccentric roller on it to rotate, driving the slide plate to move up and down. When the chute on the skateboard is low, a separate cigarette is filled into the chute. When the chute is at a high position, the cigarette automatically detaches from the chute to form a unit body and enters the full-appearance imaging device through the transition plate. The structure of the cigarette unitization device is shown in **Figure 9**.

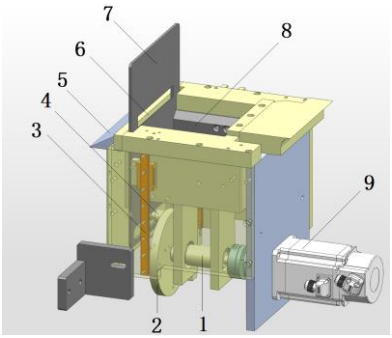

Figure 9. Unit discrete device; 1: rotating shaft; 2: wheel; 3: slide rail; 4: eccentric roll; 5: transition plate; 6: inclined slot; 7: sliding plate; 8: transition chamber; 9: electromotor.

During the unitization of the cigarette by the cam mechanism, the chute of the skateboard transports the cigarette from bottom to top, and the relationship between the stroke of the skateboard and the radius of the roller movement trajectory is $h_1 = 2r$. The position relationship of the motion process is shown in **Figure 10**.

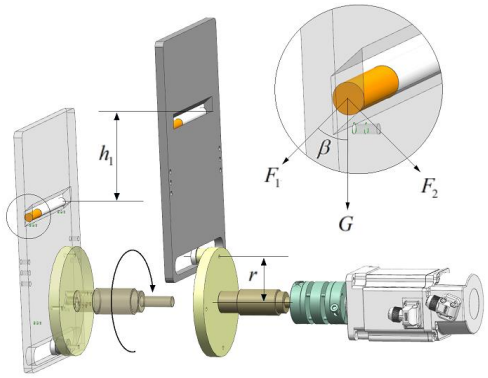

Figure 10. The movement relation between the runner chute mechanism and cigarette.

When the slot is at its lowest, the sloping bottom surface of the chute makes it easier for the cigarette to enter the chute. When the chute is at its highest, the cigarette sticks come out of the lower side of the chute. The process of entering or exiting requires reaction time, so the chute needs to pause in the high and low positions, and the pause time is greater than the sliding movement of the cigarette, that is:

$$F_1 = G \times \cos\beta \tag{14}$$

$$F_a = F_1 - F_2 \times \mathrm{u} \tag{15}$$

$$t = \sqrt{2\mathrm{S}/a} \tag{16}$$

$$s = w/\cos\beta \tag{17}$$

$$a = F_a/\mathrm{m} = (G \times \cos\beta - \mathrm{G} \times \sin\beta \times \mathrm{u})/\mathrm{m} \tag{18}$$

The following formula can be deduced:

$$t=\sqrt{2w/\cos\beta/(G\times\cos\beta-G\times\sin\beta\times \mathrm{u})/\mathrm{m})} \tag{19}$$

$$T>t \tag{20}$$

where F_1 is the gravitational component parallel to the slope, N; F_2 is the gravitational component perpendicular to the beveled plane, N; u is the coefficient of friction, m is the weight of the cigarette, g; β is the angle between the bevel and the vertical direction, (°); F_a is the resultant force of the tobacco in the parallel inclined direction, N; a is the displacement acceleration, m/s^2; w is the width of the skateboard, m; S is displacement length, m; t is the time of the motion, s; T is the dwell time of the chute, s.

From Equations (19) and (20), it can be concluded that the length of time for the cigarette to slide out is related to the width of the skateboard, the angle of the chute, and the friction coefficient. Considering the smoothness of the cigarette movement process, the chute angle should be in the range of 20°–40°. In this research, 20°, 30°, and 40° were selected for comparative tests.

2.3.3. Design of cigarette storage device

The conditions required for the supply of cigarettes are huge storage capacity and a continuous supply of cigarettes, so the belt conveying method is selected to cooperate with the storage to form a stable flow input. The cigarettes are neatly arranged in the storage bin, and the lower cigarettes are transported forward by the belt into the cigarette unitization device. The design of the cigarette storage device is shown in **Figure 11**.

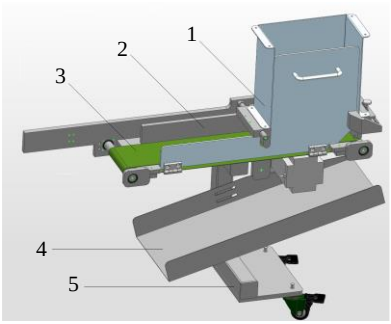

Figure 11. Device for storing and supplying cigarettes, 1: storage bin of cigarette; 2: baffle plate; 3: conveyor belt; 4: the trough for cigarette crumbs; 5: sliding bracket.

2.3.4. Design of sorting device

After the cigarette is inspected, the cigarette with a defective appearance needs to be picked out. Because of the small weight and low density of cigarettes, the use of wind rejection will make the cigarette stress state unstable, so the output method of the sub-channel is selected for cigarette sorting. The design of the sorting device is shown in **Figure 12**. An active channel is set at the end of the output channel, and a return spring is used to connect the active channel to the fixed mechanism. Through the telescopic action of the cylinder, the opening and closing of the active channel are controlled to form different output channels, and the normal cigarette stick and the defective cigarette stick are output through different channels, and finally achieve the effect of classification.

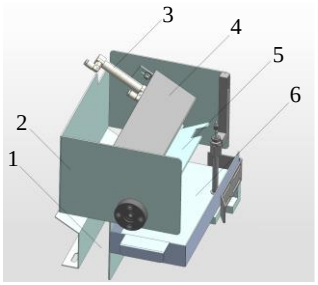

Figure 12. The sorting device, 1: the drop path of a cigarette; 2: guard shield; 3: cylinder; 4: baffle plate; 5: the convertible channel; 6: trough of samples.

2.3.5. Design of deep learning algorithm model

There are many varieties of cigarettes to be detected, and the defects in the cigarettes are various and small. Therefore, many samples are required for model training. In order to use a limited sample training set for high-quality model training, YOLOV4 was improved in several parts to adapt to the characteristics of small defect area, multiple types, and defect repulsion. The algorithm model structure of YOLOV4 is shown in **Figure 13**[24].

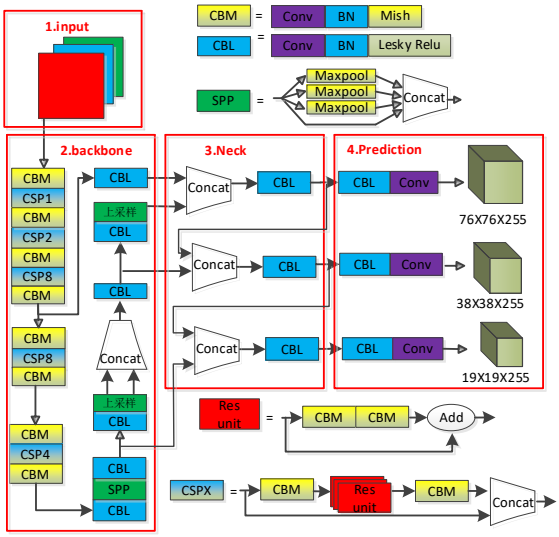

Figure 13. The Algorithm model for YOLOV4.

When training a YOLOV4 algorithm on optical pictures, a large number of sample data inputs are required[25]. However, there are many sizes and types of defects in cigarettes, many defect samples are difficult to provide for model training. Therefore, OpenCV is used to transform the darknet source code and add new data augmentation methods. Detection target areas are extracted from the marked image set and classified with defects[26]. The defective image is deformed, rotated, and changed in size, randomly fused into other images, and then marked as defective in the corresponding area of the newly fused image. Normal images are randomly blended into the new album and marked as correct. The data augmentation method is used to increase the sample data and improve the model training quality.

YOLOV4's backbone network CSPDarknet53 was replaced with improved HourglassNet. HourglassNet can make full use of the characteristics of feature images with each size, greatly improving the accuracy of the model. However, HourglassNet also increases the amount of computing, even with reference to dense network denseness, there are still problems such as difficult training, slow training speed, and high configuration consumption[27]. Considering the different influences of different

size features on the final result, the feature influence factor β is introduced to improve the DarkNet backpropagation, so as to improve the effectiveness of backpropagation. The output h of each layer of the small hourglass module is convolved by 1 × 1, and then the output $h1$ is obtained. While reducing the dimensionality, a layer of nonlinear output is added, that is, multiplying the output $h1$ by β to get $h2$. $h2$ is fused with the input part of the next layer of the hourglass network, and the result obtained is fed into the next layer of the network. HourglassNet, which is introduced into the feature impact factor β, is represented as β-HourglassNet.

In an area on the surface of the cigarette stick, at most one type of defect can be determined according to the requirements of defect detection, so different defects are mutually exclusive and do not intersect in the same area. The SoftMax used in YOLOhead produces multiple different recognition conclusions for the same regional feature when activated, so the SoftMax is replaced by sigmoid. The darknet source code is modified to classify each prediction box in two so that each region has at most one defect.

3. Results

Visual inspection equipment for the full appearance of cigarettes was manufactured and experimented. The non-destructive operation and image quality of cigarettes on the machine were tested. And the accuracy of the deep learning algorithm for defect classification was verified.

3.1. Configuration and conditions of the experiment

The experiment was completed in the quality inspection room of a cigarette factory, and the cigarette with the specification φ5.4 × 100 was selected as the experimental object, and the LED strip light source of Hikvision 5CAM23-MV-CA013-20GC industrial camera, Zhonglian Kechuang lens VM06012MP, and SWB-250-40-W was used as the equipment imaging hardware. The test machine is shown in **Figure 14**.

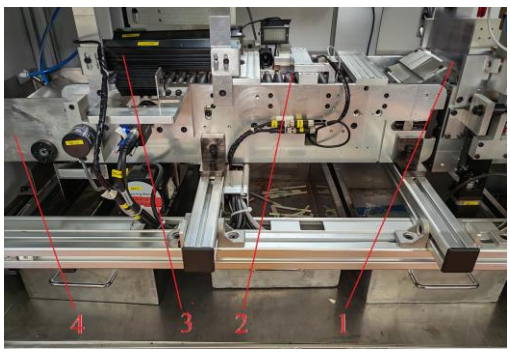

Figure 14. Test machine and test cigarette, 1: a device for forming units; 2: full appearance imaging device; 3: assembly of camera and light; 4: sorting device.

3.2. Tests of key parameters for equipment operation

The process analysis of the testing equipment shows that the cigarette unitization device and sorting device have a great influence on the conveying state of the cigarette stick, and their poor operation will cause wrinkles or damage to the surface of the cigarette. Therefore, the influencing factors of the two key devices were tested orthogonally.

3.2.1. Experiments of cigarette unitization device

During the operation of the unitization device, if the operating parameters do not match, it will

cause tilt and offset of the cigarette stick (as shown in **Figure 15**), which will affect the effectiveness of detection. The three main factors affecting the flow stability of the cigarette branch are the angle of the tilt of the transition plate, the angle of the bottom surface of the chute, and the displacement speed of the roller. The orthogonal test of the three factors is carried out, the test factor coding is shown in **Table 2**, the test scheme and results are shown in **Table 3**, and the analysis of variance for the test results is shown in **Table 4**.

Table 2. Coding table of experimental factors and levels.

Code	Lifting speed of the sliding plate/A/(m/s)	Angle of transition plate/B/(°)	Roller speed/C/(m/s)
1.68	0.23	13	0.03
1	0.3	20	0.04
0	0.4	30	0.05
−1	0.5	40	0.06
−1.68	0.57	47	0.67

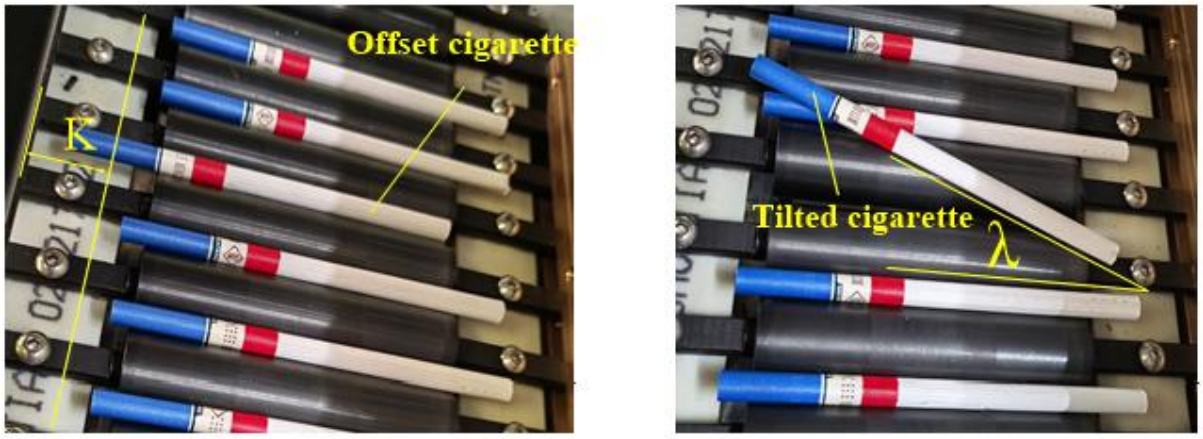

Figure 15. Abnormal operation state of cigarette, **(a)** diagram of an offset cigarette; **(b)** diagram of a tilted cigarette.

$$S = \frac{N1 - N2}{N1} \times 100\% \tag{21}$$

$$Q1 = \frac{\sum_{i}^{10} S_i}{10} \tag{22}$$

$$M = \frac{N1 - N3}{N1} \times 100\% \tag{23}$$

$$Q2 = \frac{\sum_{i}^{10} M_i}{10} \tag{24}$$

where $N1$ is the number of experimental samples; $N2$ is the number of cigarettes tilted; $N3$ is the number of cigarettes with an offset k of more than 2.5 mm (offset k greater than 2.5 mm affects the quality of images); S is the non-tilt rate,%; $Q1$ is the average non-tilt rate,%; M is the of non-offset rate, %; $Q2$ is the average of non-offset rate, %.

Table 3. Experimental scheme and results.

Number	Factors			Non-tilt rate *Q*1/%	Non-offset rate *Q*2/%
	A/(m/s)	B/(°)	C/(m/s)		
1	0.3	20	0.04	85	96
2	0.5	20	0.04	88	93
3	0.3	40	0.04	95	99
4	0.5	40	0.04	93	97
5	0.3	20	0.06	87	92
6	0.5	20	0.06	86	91
7	0.3	40	0.06	91	94
8	0.5	40	0.06	92	89
9	0.23	30	0.05	85	98
10	0.57	30	0.05	88	85
11	0.4	13	0.05	93	89
12	0.4	47	0.05	98	90
13	0.4	30	0.03	94	97
14	0.4	30	0.07	83	88
15	0.4	30	0.05	99	91
16	0.4	30	0.05	100	91
17	0.4	30	0.05	98	92
18	0.4	30	0.05	91	94
19	0.4	30	0.05	98	93
20	0.4	30	0.05	100	90

Table 4. Variance analysis.

Source of variation	Non-tilt rate/*Q*1					Non-offset rate/*Q*2				
	Sum of squares	Degree of freedom	Mean square	*F*	*P*	Sum of squares	Degree of freedom	Mean square	*F*	*P*
Model	459.82	9	51.09	4.51	0.0138**	186.97	9	20.77	3.25	0.0403**
A	2.70	1	2.70	0.24	0.6361	79.51	1	79.51	12.43	0.0055***
B	81.44	1	81.44	7.18	0.0231**	5.49	1	5.49	0.86	0.3760
C	62.46	1	62.46	5.51	0.0408**	76.86	1	76.86	12.01	0.0061***
AB	1.13	1	1.13	0.10	0.7592	1.13	1	1.13	0.18	0.6839
AC	0.13	1	0.13	0.01	0.9185	0.13	1	0.13	0.02	0.8916
BC	3.12	1	3.12	0.28	0.6110	6.13	1	6.13	0.96	0.3510
A^2	233.21	1	233.21	20.57	0.0011***	3.31	1	3.31	0.52	0.4887
B^2	10.91	1	10.91	0.96	0.3497	0.71	1	0.71	0.11	0.7464
C^2	142.91	1	142.91	12.60	0.0053***	5.08	1	5.08	0.79	0.3938
Residual	113.38	10	11.34			63.98	10	6.40		
Lack of fit	56.04	5	11.21	0.98	0.5097	53.15	5	10.63	4.91	0.0528
Error	57.33	5	11.47			10.83	5	2.17		
Total variance	573.20	19				250.95	19			

According to the analysis of variance of the experimental results in **Tables 2–4**, it can be seen that both factor *B* and factor *C* have a significant effect on the non-tilt rate *Q*1 of tobacco ($P < 0.05$), while the quadratic term of *A* and the quadratic term of *C* has a very significant effect ($P < 0.01$), and the influence of the remaining factors was not significant ($P > 0.1$). Factors *A* and *C* had a significant effect on the non-offset index of cigarettes ($P < 0.01$), while the influence of the remaining factors was not significant ($P > 0.1$).

3.2.2. Experiment of sorting device

After the cigarette is detected, the defective cigarette and the normal cigarette are output separately, and the channel conversion process should be rapid to avoid the two types of cigarette being not effectively diverted. At the same time, the conversion action should be gentle to avoid the impact of the movement of the channel on the cigarette. The key influencing factors are the speed of the cylinder's telescopic action and the elastic coefficient of the return spring. With the goal of no damage to the cigarette, the cylinder telescopic speed and spring elasticity coefficient were experimentally analyzed. A group of 200 cigarettes was tested with two factors and three levels. The test code is shown in **Table 5**, the test scheme and results are shown in **Table 6**, and the ANOVA is shown in **Table 7**.

Table 5. Coding table of experimental factors and levels.

Code	Speed of cylinder expansion and contraction *D* (mm/s)	Coefficient of elasticity of spring *E* (N/mm)
1	116.5	5.8
2	100	5
3	60	3
4	20	1
5	3.4	0.2

Table 6. Experiment scheme and results.

Number	Factors		Cigarette damage rate (*Q*3)/%
	D	*E*	
1	20	1	2
2	100	1	11
3	20	5	5
4	100	5	10
5	3.4	3	2
6	116.5	3	8
7	60	0.2	8
8	60	5.8	12
9	60	3	2
10	60	3	1
11	60	3	3
12	60	3	2
13	60	3	2

Table 7. Variance analysis.

Source of variation	Sum of squares	Degree of freedom	Mean square	*F*	*P*
Model	184.33	5	36.87	32.37	0.0001***
D	63.20	1	63.20	55.49	0.0001***
E	7.33	1	7.33	6.43	0.0389**
DE	4.00	1	4.00	3.51	0.1031
D^2	13.15	1	13.15	11.55	0.0115**
E^2	104.46	1	104.46	91.71	0.0001***
Residual	7.97	7	1.14		
Lack of fit	5.97	3	1.99	3.98	0.1076
Error	2.00	4	0.50		
Total variance	192.31	12			

According to the results of ANOVA in **Table 7**, it can be seen that factor *D* and the quadratic term of factor *E* had an extremely significant effect on the cigarette damage rate *Q*3 ($P < 0.01$), while factor *E* and the quadratic term of factor *D* had a significant effect on it ($P < 0.05$).

3.3. Experiment for acquiring images

3.3.1. Images of the circumferential surface on cigarettes

Whether the camera can capture 360° surface images of cigarettes is the key to the effective function of the equipment. Therefore, the cigarette surface imaging is examined to ensure complete coverage of the image. φ5.4 × 100 size cigarettes are selected and divided into groups of 100, and the surface of the cigarettes is separated by line marks on the surface of the cigarettes at 120° intervals. Cigarettes were photographed in three locations with a spacing of $(n + 2/3)\pi$, then three images of one cigarette are combined to verify that the pictures can form a 360° surface of the cigarette's circumferential surface. The test device and cigarette images are shown in **Figure 16**.

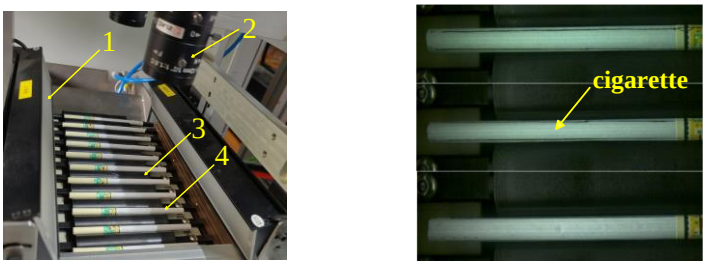

(a) **(b)**

Figure 16. Image action test in three working positions, **(a)** device for experiment; **(b)** images of cigarettes; 1: light source; 2: camera; 3: roller; 4: cigarette.

3.3.2. Imaging experiments with combinations of light parameters

There are many defect detection items on the circumferential surface of the cigarette, and high-quality images of the circumferential surface of the cigarette stick are very important for detection, so imaging requires a good lighting environment. In this research, the three angles of the light source: 0 degree, 10 degree, 20 degree and three height differences between light source and cigarette: 10 mm, 20 mm, 30 mm were combined for comparative experiment, obtaining optimal lighting condition. The experiment is shown in **Figure 17**, and the photographs and pixel histograms are shown in **Figure 18**.

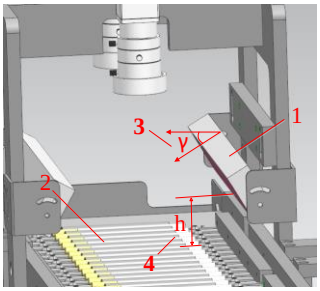

Figure 17. The experiment of lighting parameter, 1: light source; 2: cigarette; 3: the angle between the light source and the horizontal plane; 4: the height between the light source and the cigarette.

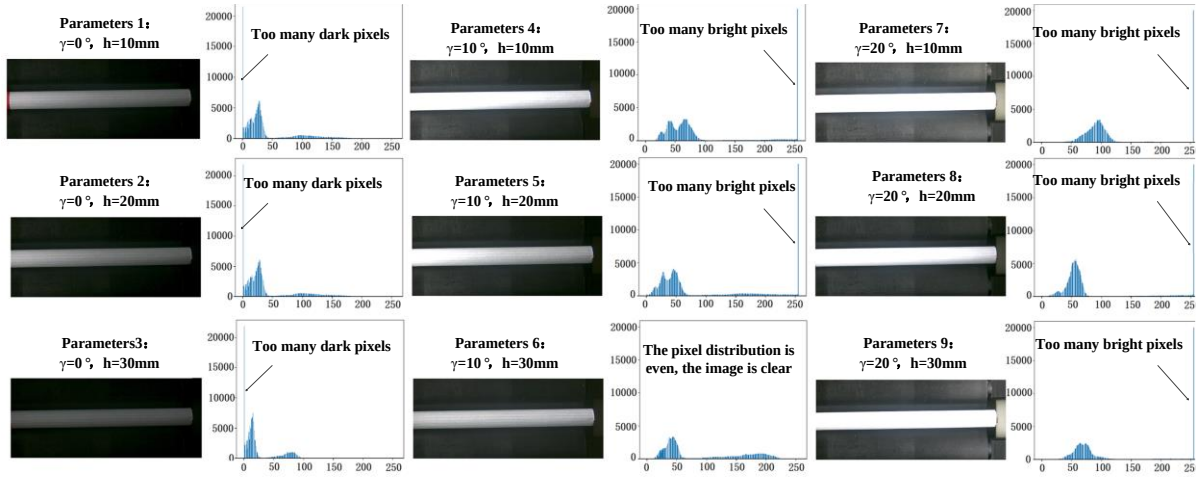

Figure 18. Relationship between effect of cigarette picture and lighting parameters.

3.4. Verification experiment of defect detection algorithm model

3.4.1. Experiments on the recognition ability of β-HourglassNet-yoloV4

The configuration used in the experiment was: TensorFlow-GPU 2.3 deep learning framework, processor Intel-i7 9700, graphics card NVIDIA TESA V100 32GB, operating system WIN10, driver 496.49.

An important indicator of the training effect of a deep learning model is the loss value. Under the same training conditions, the smaller the loss value of model training, the better the model training effect. CSPDarknet53-yoloV4, HourglassNet-yoloV4, and β-HourglassNet-yoloV4 were trained with a training image set of 2000, and the effects were compared. After 20,000 iterations, the loss values of CSPDarknet53-yoloV4, HourglassNet-yoloV4, and β-HourglassNet-yoloV4 are Respectively 0.27, 0.1 and 0.06. After being trained, the detection speed and CPU usage of the three models are shown in **Table 8**.

The training results in **Table 8** show that the detection speed of β-HourglassNet-yoloV4 is slightly lower than that of HourglassNet-yoloV4 and CSPDarknet53-yoloV4 for the same image size, while the average CPU usage rate is 24%, higher than HourglassNet-yoloV4 and CSPDarknet53-yoloV4.

Table 8. Training results of different models.

Models	The size of the picture/pixel	Detection speed/(frame/s)	Average CPU usage/(%)
CSPDarknet53-yoloV4	416 × 320	6.3	19%
HourglassNet-yoloV4	416 × 320	4.7	21%
β-HourglassNet-yoloV4	416 × 320	4.3	24%

3.4.2. Detection experiment of cigarette defects

There are many kinds of defects on the surface of cigarettes, and in this experiment, four main defects were selected to verify the recognition effectiveness of the deep learning algorithm, including end folds, clamped cigarette fragments, punctures, and wrinkles. 500 defective cigarettes were selected for image acquisition and image enhancement, and then 500, 1000 and 2000 sample images were used to train CSPDarknet53-yoloV4, HourglassNet-yoloV4 and β-HourglassNet-yoloV4 respectively. Cigarettes with defects were detected on the device and the results are shown in **Figure 19**. The detection accuracy and classification accuracy of the three models were counted and compared, and the results are shown in **Tables 9** and **10**.

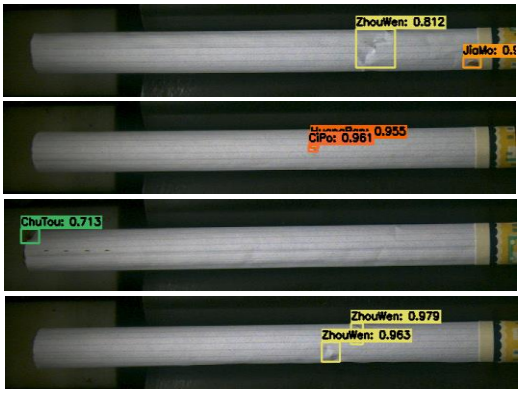

Figure 19. Classification of defect detection results.

It can be seen from **Table 9** that the accuracy of defect detection of the three models under the training of 500, 1000, and 2000 sample sizes respectively has obvious differences. CSPDarknet53-yoloV4 has the lowest defect detection accuracy after training with the same sample size, and the defect detection accuracy of HourglassNet-yoloV4 is higher than that of CSPDarknet53-yoloV4. β-HourglassNet-yoloV4 has the highest quasi-accuracy, and the accuracy of defect detection under the three training sample sets is 96%, 97.6%, and 98%, respectively.

Table 9. Detection accuracy of cigarette defects under different training models.

Models	**Detection accuracy of cigarette defects (map)**		
	Sample size: 500	**Sample size: 1000**	**Sample size: 2000**
CSPDarknet53-yoloV4	77%	84%	86%
HourglassNet-yoloV4	82%	87%	91%
β-HourglassNet-yoloV4	96%	97.60%	98%

Table 10. Classification accuracy of cigarette defects under different training models.

Models	**Classification accuracy of cigarette defects (map)**		
	Sample size: 500	**Sample size: 1000**	**Sample size: 2000**
CSPDarknet53-yoloV4	71%	78%	83%
HourglassNet-yoloV4	74.50%	82%	86%
β-HourglassNet-yoloV4	83%	91.60%	95.40%

In addition to being identified, cigarette defects also need to be accurately classified so that various defects can be counted and analyzed. As shown in **Table 10**, β-HourglassNet-yoloV4 can achieve defect

classification accuracy of 83%, 91.6%, and 95.4% under the three training results of 500, 1000, and 2000, respectively, higher than the classification accuracy of CSPDarknet53-yoloV4 and HourglassNet-yoloV4.

4. Discussion

4.1. Preferred parameters for equipment operation

4.1.1. Parameters of cigarette unitization device

The experimental data were processed with Design-Expert11 software, then the results were presented in the form of response surfaces and analyzed to obtain the best scheme. The factor response surface curve is shown in **Figures 20–25**. As shown in **Figure 20**, when the lifting speed of skateboard A is constant, the non-tilt rate *Q*1 gradually increases with the increase of the tilt angle of the transition plate *B*. When the tilt angle *B* of the transition plate is constant, the change trend of non-tilt rate *Q*1 is: as the lifting speed *A* of the skateboard increases, it rises first and then falls. As shown in **Figure 21**, when the lifting speed *A* is constant, the non-tilt rate *Q*1 gradually decreases with the increase of the roll displacement speed *C*. When the roller displacement speed *C* is constant, the non-tilt rate *Q*1 changes slowly with the increase of the skateboard lifting speed *A*. Therefore, in order to improve the non-tilt rate *Q*1, the optimal range of skateboard lifting speed *A* is 0.35–0.45 m/s.

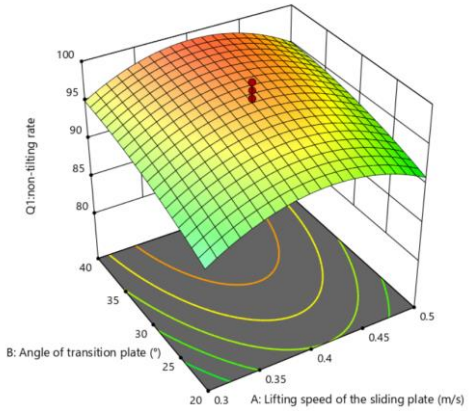

Figure 20. Response surface of factor *A* and factor *B*.

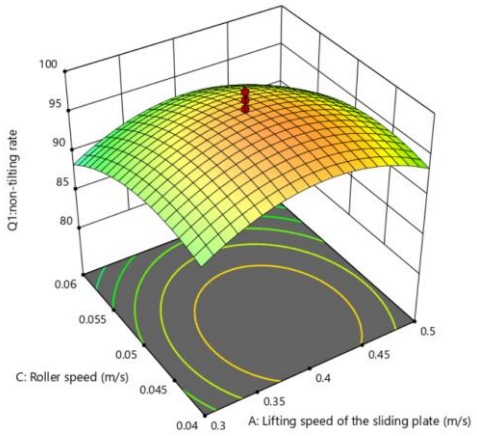

Figure 21. Response surface of factor *A* and factor *C*.

As shown in **Figure 22**, when the tilt angle *B* of the transition plate is constant, the non-tilt rate *Q*1 decreases with the increase of the roll displacement speed *C*, and the optimal range of the roll

displacement speed *C* is 0.04–0.045 m/s. When the roller displacement speed *C* is constant, non-tilt rate *Q*1 is positively correlated with the tilt angle *B* of the transition plate, and the optimal range of the tilt angle of the transition plate is 35°–40°.

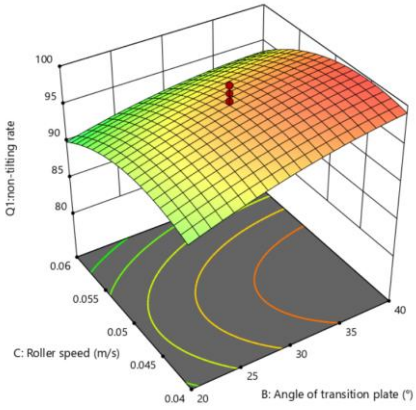

Figure 22. Response surface of factor *B* and factor *C*.

As shown in **Figure 23**, when the tilt angle *B* of the transition plate is constant, the non-offset rate *Q*2 increases significantly with the increase of the lifting speed *A* of the skateboard. When the value of the lifting speed *A* of the skateboard is constant, the change of the tilt angle *B* of the transition plate has no obvious effect on the non-offset rate *Q*2. As shown in **Figure 24**, when the tilt angle *B* of the transition plate is constant, the non-offset rate *Q*2 increases significantly with the increase of the roll displacement speed *C*, and the change of the tilt angle *B* of the transition plate has no regular effect on the non-offset rate *Q*2.

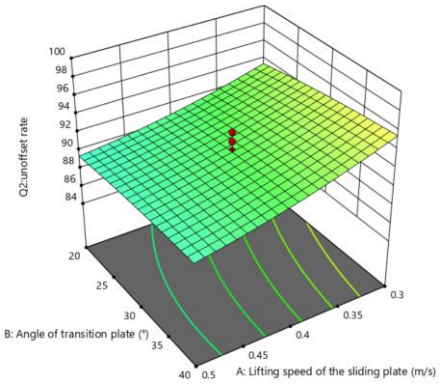

Figure 23. Response surface of factor *A* and factor *B*.

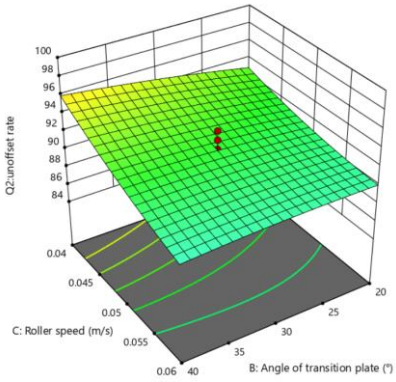

Figure 24. Response surface of factor *B* and factor *C*.

As shown in **Figure 25**, when the lifting speed *A* of the skateboard is constant, the non-offset rate *Q*2 shows a downward trend with the increase of the roll displacement speed *C*, and the optimal range of the roller displacement speed is 0.04–0.045 m/s. When the roller displacement speed *C* is constant, the non-offset rate *Q*2 shows a downward trend with the increase of skateboard lifting speed *A*, and the optimal range of skateboard lifting speed is 0.3–0.35 m/s.

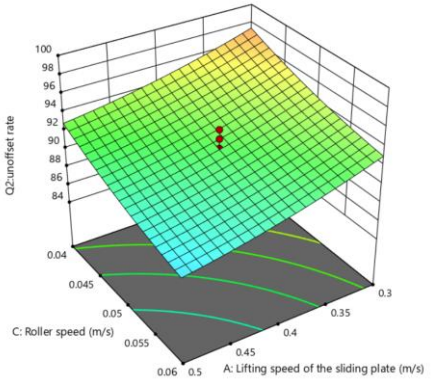

Figure 25. Response surface of factor *A* and factor *C*.

Among the three factors, the selection of skateboard lifting speed *A* is mainly based on the influence of non-offset rate *Q*2, and the second is the influence on the non-tilt rate *Q*1, so 0.3 m/s is selected to improve the non-offset rate; The selection of tilt angle *B* of the transition plate is based on the influence of non-tilt rate *Q*1, and 40° is selected to improve *Q*1; The roller displacement velocity *C* has a significant effect on the non-tilt rate, and an extremely significant effect on the non-offset rate *Q*2, and both the *Q*1 and *Q*2 were negatively correlated with the roll displacement speed. Considering the balance of non-tilt rate, non-offset rate, and the high efficiency of the equipment, the roller displacement speed is selected to be 0.045 m/s. Testing with the selected parameter combination, the non-tilt reaches 100%, and the non-offset rate reaches 99.5%, which can meet the photostability of cigarette detection.

4.1.2. Parameters of the experiment of sorting device

The response surface obtained by the analysis in Design-Expert11 is shown in **Figure 26**, and the one-way response curve is shown in **Figure 27**. The cigarette damage rate *Q*3 increases with the increase of the cylinder expansion speed *D*. When the cylinder telescopic speed *D* is constant, the cigarette damage rate *Q*3 first decreases and then rises with the increase of spring elasticity coefficient *E*. The optimal range of spring elasticity coefficient is 2.5–3.5 N/mm. From the test results and the response surface, it can be seen that the influence of factor *D* on the damage rate is the main factor, and factor *E* is the secondary factor. The cigarette damage rate decreases significantly with the decrease of cylinder telescopic speed *D*, but too slow cylinder telescopic speed will affect the conversion of the channel, so the cylinder speed is selected to be 20 mm/s. According to the response curve range, the elastic coefficient *B* was selected as 3 N/mm, and the selected parameter combination was used to experiment, the resulting tobacco damage rate was 0.

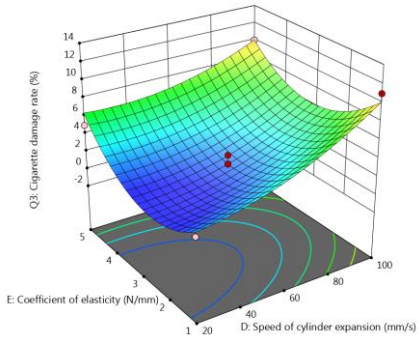

Figure 26. Response surface of factor *D* and factor *E*.

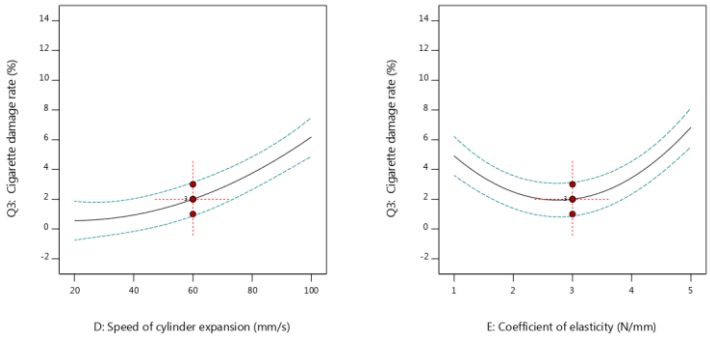

Figure 27. Response curve of factor *D* and factor *E*.

4.2. Preferred parameters for acquiring images

4.2.1. Parameter of cigarette unitization device

As shown in **Figure 16**, the results show that the range of each picture is larger than the 120-degree circumference of the cigarette, and the image edges of the first station photo, the second station photo, and the third station photo coincide. The combination of the three images can cover the 360-degree circumference of the cigarette stick, which can fully show the circumferential surface of the cigarette.

4.2.2. The illumination parameters of the light source

As shown in **Figure 18**, the abscissa of the histogram represents the luminance range, and the ordinate represents the number of pixels. When the angle between the light source and the horizontal plane is 0°, the image is dark, and the corresponding histogram shows that there are too many points with a brightness value of 0. When the angle between the light source and the horizontal direction is 20°, the picture light is too bright, and the corresponding histogram shows that there are too many pixels with a brightness greater than 250. Therefore, a γ of 0° or 20° is not conducive for imaging. When the angle between the light source and the horizontal plane is 10°, the brightness of the picture is moderate, but when the h is 10 mm or 20 mm, bright spots are easy to form, and the histogram shows that the distribution of pixels is uneven, which is not conducive to imaging. When h is 30 mm, the photo features are clear, and the histogram shows that the transition between pixel value and pixel distribution is smooth, which is conducive to imaging the circumferential surface of cigarettes.

4.3. Defect detection capability

As showed in **Table 11**, the detection speed, defect detection accuracy and classification accuracy of the three models under the condition of 2000 training samples are counted and compared, and the results show that β-HourglassNet-yoloV4 has obvious advantages in detection accuracy.

Table 11. Comparison of model performance parameters.

Models	Detection speed/(*f*/*s*)	Detection accuracy/%	Classification accuracy/%
CSPDarknet53-YOLOv4	6.3	86	83
HourglassNet-YOLOv4	4.7	91	86
β-HourglassNet-yoloV4	4.3	98	95.40

5. Conclusions

Based on the shape and physical characteristics of cigarettes, a full-vector visual inspection equipment for cigarette sticks was developed, which realized the unitization of batch cigarettes, imaged the full appearance of individual cigarettes, detected and classified the appearance defects of cigarettes, and sorted normal cigarettes and defective cigarettes.

The three factors affecting cigarette movement were orthogonally experimented with, and the experimental results were analyzed by variance, and the optimal combination of the three factors was obtained: the lifting speed of the skateboard was 0.3 m/s, the angle of the transition plate was 40°, and the roller displacement speed was 0.045 m/s. The orthogonal experiments were carried out on the two factors causing cigarette damage on the sorting device, and the optimal combination was obtained: the cylinder telescopic speed was 20 mm/s and the spring coefficient was 3 N/s; Analysis of the images of the cigarette on the full-appearance imaging device shows that the cigarette images of the three stations spaced at a distance of $\pi(n + 1/3)$ can fully show the full circumferential surface of cigarettes. The experiment on the angle and height of the light source shows that the optimal combination is: the angle of the light source is 10°, and the height difference between the light source and the cigarette stick is 30 mm, which is conducive to high-quality imaging.

According to the defect detection comparison of CSPDarknet53-yoloV4, HourglassNet-yoloV4, and β-HourglassNet-yoloV4, the results show that β-HourglassNet-yoloV4 has obvious advantages, and the defect detection accuracy rate reaches 98% and the defect classification accuracy can reach 95.4% under the condition of a training sample size of 2000 pictures.

In this paper, the detection equipment of cigarette sticks is researched and experimented with, and the results prove that it has excellent defect detection ability, which provides a reference for the visual inspection of cylindrical objects.

Author contributions

Conceptualization, SJ and FW; methodology, ZZ; software, JL; validation, SJ, ZL and JL; formal analysis, JL; investigation, CW; resources, ZZ; data curation, SJ; writing—original draft preparation, SJ; writing—review and editing, FW; visualization, KX; supervision, JL; project administration, KX; funding acquisition, KX. All authors have read and agreed to the published version of the manuscript.

Conflict of interest

The authors declare no conflict of interest.

References

1. Phiri J, Malec K, Majune SK, et al. Durability of Zambia's agricultural exports. *Agriculture* 2021; 11(1): 73. doi: 10.3390/agriculture11010073
2. Akhtar MN, Ansari E, Alhady SSN, et al. Leveraging on advanced remote sensing- and artificial intelligence-based technologies to manage palm oil plantation for current global scenario: A review.

Agriculture. 2023; 13(2): 504. doi: 10.3390/agriculture13020504
3. Xiong Y, Li Y, Wang C, et al. Non-destructive detection of chicken freshness based on electronic nose technology and transfer learning. *Agriculture* 2023; 13(2): 496. doi: 10.3390/agriculture13020496
4. Wang X, Zhi M. Summary of object detection based on convolutional neural network. In: Proceedings of the Eventh International Conference on Graphics and Image Processing (ICGIP 2019); 12–14 October 2019; Hangzhou, China.
5. Ma D, Tang P, Zhao L. Review of data augmentation for image in deep learning. *Journal of Image and Graphics* 2021; 26(3): 487–502.
6. Ren Z, Fang F, Yan N, et al. State of the art in defect detection based on machine vision. *International Journal of Precision Engineering and Manufacturing-Green Technology* 2021; 9(2): 661–691. doi: 10.1007/s40684-021-00343-6
7. Lee PJ, Bui TA, Yao SR. Improve the HEVC algorithm complexity based on the visual perception. In: Proceedings of the 2019 IEEE International Conference on Consumer Electronics (ICCE); 11–13 January 2019; Las Vegas, NV, USA. pp. 1–4, doi: 10.1109/ICCE.2019.8662038
8. Jin Z, Zhong F, Zhang Q, et al. Visual detection of tobacco packaging film based on apparent features. *International Journal of Advanced Robotic Systems* 2021; 18(3): 172988142110248. doi: 10.1177/17298814211024839
9. Hu Y, Luo X, Gao Z, et al. Curve skeleton extraction from incomplete point clouds of livestock and its application in posture evaluation. *Agriculture* 2022; 12(7): 998. doi: 10.3390/agriculture12070998
10. Yu JJ, Zhou J, Xue R. Weld surface quality detection based on structured light and illumination model. *Chinese Journal of Lasers* 2022; 49(16): 170–178.
11. Tian X, Wang Z, Wang JX. Text detection of food labels based on semantic segmentation. *Transactions of the Chinese Society for Agricultural Machinery* 2020; 51(08): 336–343.
12. Zhao B. *Research on the Key Technology of Drug Packaging Detection Based on Machine Vision*. Liaoning University of Technology; 2022.
13. Xiao C, Qiu H. A count measurement method for low contrast stacked sheets in machine vision. *Journal of Hunan University (National Science)* 2018; 45(4): 122–128.
14. Madessa AH, Dong J, Dong X, et al. Leveraging an instance segmentation method for detection of transparent materials. In: Proceedings of the 2019 IEEE SmartWorld, Ubiquitous Intelligence & Computing, Advanced & Trusted Computing, Scalable Computing & Communications, Cloud & Big Data Computing, Internet of People and Smart City Innovation (SmartWorld/SCALCOM/UIC/ATC/CBDCom/IOP/SCI); 19–23 August 2019; Leicester, UK. pp. 406–412. doi: 10.1109/SmartWorld-UIC-ATC-SCALCOM-IOP-SCI.2019.00113
15. Liu J, Dong L, Suo X. Study on visual detection of foreign matter in groove of zirconium tube based on average template method. *Journal of Hunan University (National Science)* 2020; 44(12): 53–60.
16. Deng Y, Pu H, Hua X, Sun B. Research on lane detection based on RC-DBSCAN. *Journal of Hunan University (National Science)* 2021; 48(10): 85–92.
17. Chen X, Fang Y, Du S, et al. Rapid packaging defect detection method based on deep learning. *Machine Design and Research* 2021; 37(06): 165–169.
18. Hou B, Hu Y, Zhang P, et al. Potato late blight severity and epidemic period prediction based on Vis/NIR spectroscopy. *Agriculture* 2022; 12(7): 897. doi: 10.3390/agriculture12070897
19. Zhang Z, Zhang Z, Li J. Potato detection in complex environment based on improved YoloV4 model. *Transactions of the Chinese Society of Agricultural Engineering* 2021; 37(22): 170–178.
20. Jiang T, Zhang G, Gao J. Illumination of a cylinder block transverse hole for machine vision inspection. *Chinese Optics* 2020; 12(06): 1285–1292.
21. Xu J. *Research on Visual Inspection Algorithm for Label Defect of Cylindrical Products*. Guangzhou University; 2018.
22. Liu R. *Design and Implementation of Full-Appearance Visual Inspection System for Rotary Parts*. Shanghai University of Engineering Science; 2021.
23. Liu Z. Application of black box method in fault detection of tunneling electrical control system. *Mechanical & Electrical Engineering Technology* 2019; 48(12): 233–235.
24. Jiang D. A brief analysis of Yolov3 and Yolov4. Available online: https://zhuanlan.zhihu.com/p/143747 (accessed on 19 December 2021).
25. Wang W, Wang H, Dong Z. Deep learning data augmentation method in microscopy imaging. *Laser Journal* 2022; 43(2): 96–100.
26. Wang J, Chen X, Yang Z. Influence of different data augmentatio methods on model recognition accuracy. *Computer Science* 2019; 48(12): 233–235.
27. Fan D, Sun X, Wang Q. Multistage dense block hourglass network for human pose estimation. *Transducer and Microsystem Technologies* 2020; 39(11): 47–52.